


Plasma-assisted temporal shifts of bichromatic femtosecond laser pulses in airV. Tamulienė ,* D. Buožius, and V. Vaičaitis *Laser Research Center, Vilnius University, Saulėtekio 10, Vilnius LT-10223, Lithuania* (Received 7 December 2020; accepted 15 February 2021; published 4 March 2021)

Terahertz and third-harmonic generation by tightly focused bichromatic femtosecond pump pulses with comparable input intensities in air is studied both experimentally and theoretically. Plasma-assisted temporal shifts in the field of intense laser pulses are shown to lead to the time delay between the pump pulses in the vicinity of the focus. This delay can be compensated by the initial time delay that is evidenced by the measured as well as calculated correlation functions of the fundamental and second harmonics. The possibility to characterize the plasma channel length from the correlation function is discussed.

DOI: [10.1103/PhysRevA.103.033502](https://doi.org/10.1103/PhysRevA.103.033502)**I. INTRODUCTION**

Propagation of focused femtosecond laser pulses in air usually is accompanied by a variety of nonlinear optical phenomena, including odd-order harmonic generation [1,2], four- and six-wave mixing [3–5], spectral broadening and supercontinuum generation [6,7], etc.

On the other hand, terahertz (THz) generation in air by femtosecond bichromatic laser pulses is an important nonlinear process accompanied by beam diffraction or focusing, ionization of the medium, optical Kerr effect, and third-harmonic generation (THG); see [8,9] for the review of these effects. In this process, the focused fundamental harmonic (FH) wave overlaps with its second harmonic (SH) and either their four-wave mixing (FWM) or the currents in the laser-created plasma allows the generation of broadband THz radiation. Since the SH is generated in a nonlinear crystal from the FH, its intensity is conventionally lower than that of the FH, e.g., of the order of 10% of the FH intensity [10,11]. Therefore, most of the nonlinear effects are predetermined by the FH wave.

The rise of the THz radiation yield with the increase of the input FH energy is restricted by the intensity clamping in the ionized medium. Another possibility to intensify the THz output is to increase the input SH energy so that both the FH and SH intensities become comparable. Then, both processes leading to the THz generation—the four-wave mixing [12] and plasma currents [13,14]—should become more efficient.

In the case of two pumps with comparable energies the study of THz generation is a challenge since light filament and plasma generation are predetermined by the two pump waves and as we show in this paper plasma-assisted temporal shifts in FH and SH pulses may arise. Therefore, here we study the influence of the time delay between the FH and SH pulses on the conversion efficiency to the generated THz radiation as well as third-harmonic (TH) wave. The measured dependences acquire a maximum at the appropriate delay

value and this value is in tight connection with the generated plasma channel length. Note that even small time delays of a few femtoseconds can influence the THz yield [15].

The THz yield at comparable FH and SH intensities was studied in [16,17]. The photocurrent model developed in [16] showed the optimal phase difference between the SH and FH waves to be $\pi/2$. This phase difference causes the symmetry-broken laser field and as a consequence the nonzero drift velocity of the plasma electrons. The TH yield was shown to be phase sensitive, too [17]. In the present paper, the time delay is in tight connection with the change of the phase difference. In [18], the photocurrent model was extended for collisional plasma and the THz generation in plasma was viewed as a four-wave mixing process. On the other hand, the TH radiation generated in the filament is guided by the FH wave and the energy exchange between FH and TH takes place [19]. The FH and TH X-waves propagation at the same group velocity was shown [20,21] and it is important to take into account the tunnel ionization when estimating the group velocity theoretically [21].

Note that numerical simulation of plasma generation meets an additional obstacle: no formula for the generation rate in the two-color field for both multiphoton and tunnel ionizations is present [22]. Therefore, one should choose one of the ionization mechanisms: multiphoton or tunnel ionization. Multiphoton ionization (MPI) is appropriate at lower intensity values while tunnel ionization dominates at higher intensities. The transition is described by the Keldysh parameter $\gamma = 2\pi\tau_I/T$ where $\tau_I = \sqrt{2I_p}/E$ (it is written in atomic units; I_p is the ionization potential and E is the electric field), while T is the optical cycle. Multiphoton ionization takes place at $\gamma \gg 1$ and tunnel ionization is the ionization mechanism at $\gamma \ll 1$. At a pump wavelength of a Ti:sapphire laser of 800 nm the transition value of $\gamma = 1$ is achieved at an intensity of the order of 10^{13} W/cm². On the other hand, the increase of the intensity of the focused beam is arrested by the plasma defocusing and subsequent intensity clamping. Therefore, in this paper, we choose the multiphoton ionization mechanism and restrict our theoretical consideration to the onset of the intensity clamping. In this case, the THz radiation according

*viktorija.tamuliene@ff.vu.lt

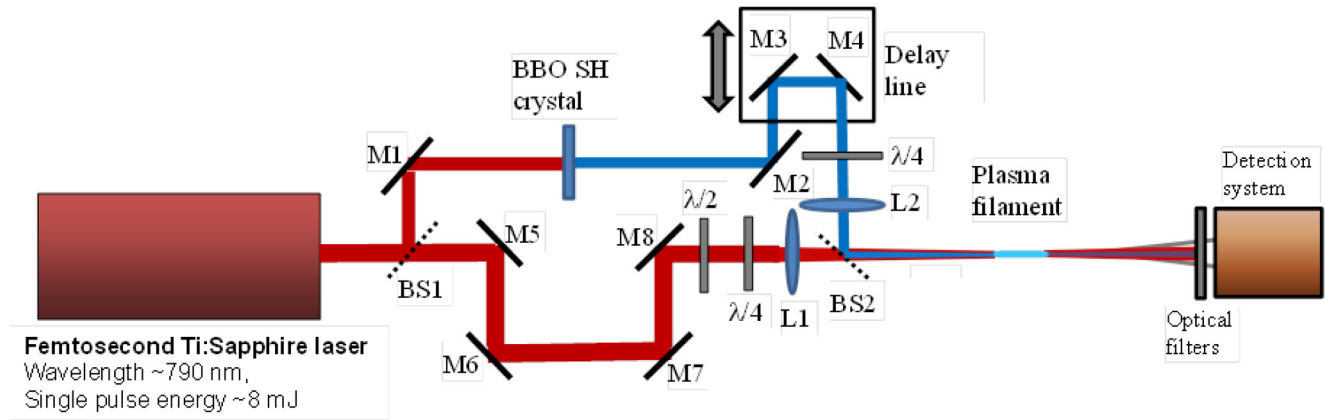


FIG. 1. Experimental setup. M1–M8, dielectric mirrors; L1 and L2, focusing lenses; $\lambda/4$, quarter-wave plates; BS1 and BS2, beam splitters; SH and FH beams are shown by blue and red-pink color, respectively.

to our model is generated only by the $\chi^{(3)}$ nonlinearity, e.g., by bound electrons. However, in the experiment, the generated THz wave may be viewed as a result of both tunnel ionization and $\chi^{(3)}$ nonlinearity of air.

The rest of the paper is organized as follows: the experimental setup and the measurement of the correlation functions are presented in Sec. II. In Sec. III, the numerical model is described and the results of the numerical simulation are presented. The experimental and theoretical results are compared in Sec. IV and the discussion on the observed effects is given. The conclusions are drawn in Sec. V.

II. MEASUREMENT OF THE THG AND THz CORRELATION FUNCTIONS

A. Experimental setup

For the experiments we have used a setup shown in Fig. 1. A primary light source was a 1-kHz repetition rate femtosecond Ti:sapphire chirped pulse amplification laser system (Legend elite duo HE+, Coherent Inc.), delivering 40–45-fs [full width at half maximum (FWHM)] light pulses centered at 790 nm with a maximal pulse energy of 8 mJ. In order to obtain bichromatic light pulses, first the laser beam was divided into two arms using a thin 50:50 beam splitter BS1. One of these beams was used for the second-harmonic generation in a 0.2-mm-thick nonlinear beta barium borate (BBO) crystal. (We estimate the SH pulse duration to be almost the same as that of the FH.) From the fundamental the SH radiation was filtered by the spectrally selective dielectric mirrors M2–M4. The power of the beams could be varied (reduced) by inserting thin partially reflecting dielectric mirrors into the beam paths. A temporal delay between the FH and SH pulses was controlled by a motorized optical delay line, and their polarizations could be changed from linear to circular using the broadband zeroth-order quarter-wave plates. Each beam was focused with a separate lens of different focal length (10 and 15 cm for the FH and SH beams, respectively). The beam radius at the FWHM was about 6.7 mm for FH and 5.9 mm for SH. Then both beams were concentrically superposed at a dichroic beam splitter BS2. Note that lengths of the plasma filaments, created by each beam separately, were quite

different. Thus, SH pulses of over a 1-mJ energy produced filaments longer than a few mm, while the focused FH pulses with an energy of about 100 μ J resulted in appearance of less than 1-mm-long plasma volumes (Fig. 2). Note also that the lengths of plasma filaments created by the SH pulses were significantly larger in comparison to those created by the FH pulses due to different lengths of lenses used to focus these beams. In addition, it is easy to see that both filaments become longer and move towards the focusing lenses, when the pulse energy is increased, which is a signature of nonlinear self-focusing of the beams in air [23–25].

When both the FH and SH pulses were temporally overlapped, a few different nonlinear processes were taking place in the plasma filament. Among others the most important are the THz radiation generation [26,27] and third-harmonic generation by FWM of the FH and SH frequencies [3]. Therefore, we have analyzed both processes: in the case of THz radiation generation the Si wafer, placed in front of the detector, was

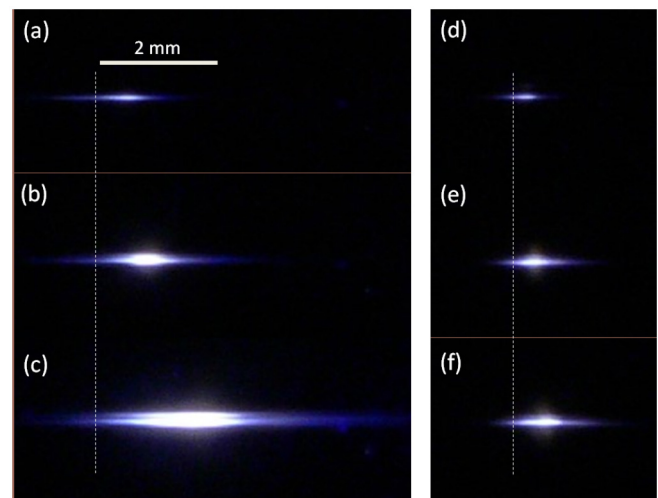


FIG. 2. Experimental results. Plasma filaments created by the SH (a), (b), (c) and FH pulses (d), (e), (f). Pulse energy was 0.11, 0.38, 1.53, 0.1, 0.3, and 0.5 mJ, respectively. (Here, the propagation takes place from the right to the left and dashed lines indicate positions of geometrical focus.)

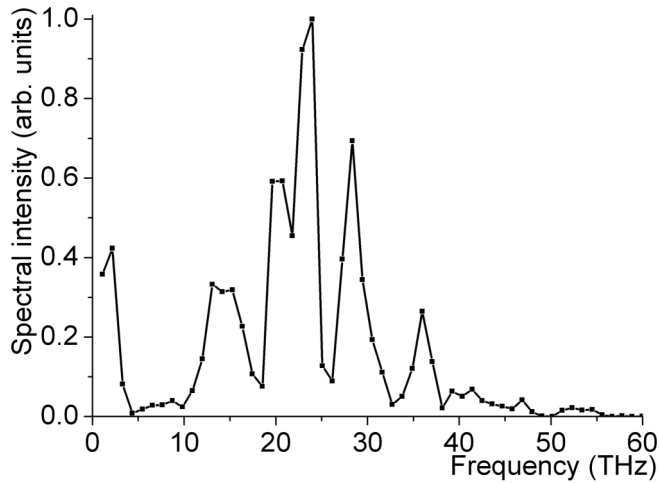


FIG. 3. Typical experimental amplitude spectrum of generated THz pulses. Modulation of the spectrum resulted from the absorption in used THz filters such as Si wafers.

used to block the pump radiation (FH and SH pulses), while in the case of THG the pump radiation was filtered using a combination of wavelength-selective dielectric and colored glass filters.

Note that for the detection of THz radiation we have used a pyroelectric detector TPR-A-65 THz (Spectrum Detector, Inc.), sensitive in the range 0.1-300THz (3000-1 μ m) with a flat response function from ≈ 3 to ≈ 100 THz. Since the divergence of generated THz radiation was about 5 deg [27], it was collimated and focused onto the detector with the help of two large aperture (2 in. in diameter) parabolic off-axis mirrors. Spectra of THz radiation were obtained from Fourier-transformed interferometric measurements and typically spanned from a few to 40 THz with the peak spectral intensity located around 25 THz (see Fig. 3).

B. Experimental results

During the experiment we have registered dependencies of THz and third-harmonic signal amplitude as a function of delay between the FH and SH pulses at various pump pulse energies. The typical registered dependencies, which in fact are the cross-correlations of the FH and SH pulses, are presented in Fig. 4. One can see that, in comparison to THz generation, the width of THG cross-correlations is larger and their positions are more strongly dependent on the pump power. Note that in some cases we have registered two-peaked THz cross-correlations [see dotted line in Fig. 4(b)], which we believe represent a temporal splitting of the SH pulse during propagation.

Another effect, which is clearly seen in Fig. 2, and was mentioned above, is the length increase and shift of the plasma filament towards the focusing lens with the pump power. Since these spatial shifts could affect the amplitude of the registered signal, during the experiment we have controlled and kept superposed loci of the plasma filaments created by the separate SH and FH pulses. Thus, even in the case of superposed plasma filaments the positions of amplitude points of THz and TH cross-correlations were clearly dependent on

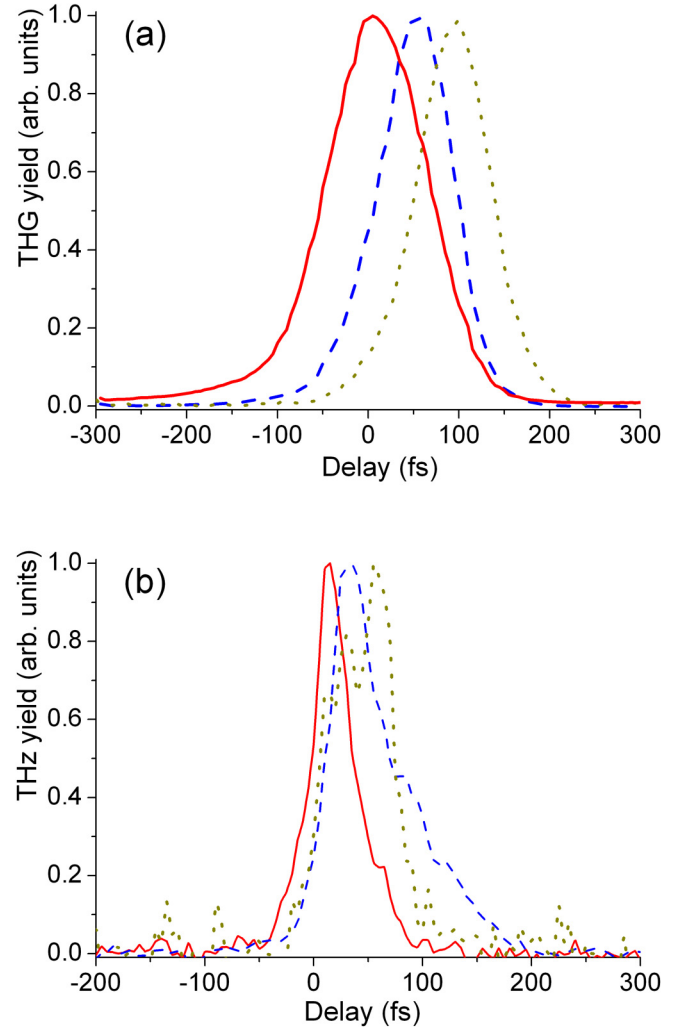


FIG. 4. Experimental results. Normalized typical THG (a) and THz (b) cross-correlations. In (a) the solid, dashed, and dotted lines correspond to FH/SH pulse energies of 0.5/0.92, 0.1/0.014, and 0.5/0.014, respectively, while in (b) these lines correspond to 0.1/0.99, 0.5/0.1, and 0.1/0.1. All energy values are given in mJ.

the pump pulse (either SH or FH) energy (compare positions of the solid, dashed, and dotted curves in Fig. 4). More detailed illustration of this effect is presented in Fig. 5. At lower SH energy both THz and THG correlation maxima move to larger delay values when the FH energy increases. At larger SH energy, the maximum stays approximately at the same position [Fig. 5(a), red line].

Note that clear dependence of the temporal TH and THz cross-correlation peak positions on the pump power implies the possible different scaling laws of THz or TH energy at different delays between the FH and SH pulses. Indeed, Fig. 6 demonstrates this phenomenon: one can see [Fig. 6(a)] that the dependencies of the overall THz energy on SH power are quite different at different delay times, i.e., if the THz signal is large at low pump energies it saturates faster with SH power and vice versa. This means that in order to maximize THz yield one should optimize the initial time delay between the pump pulses depending on their energy. The similar dependencies

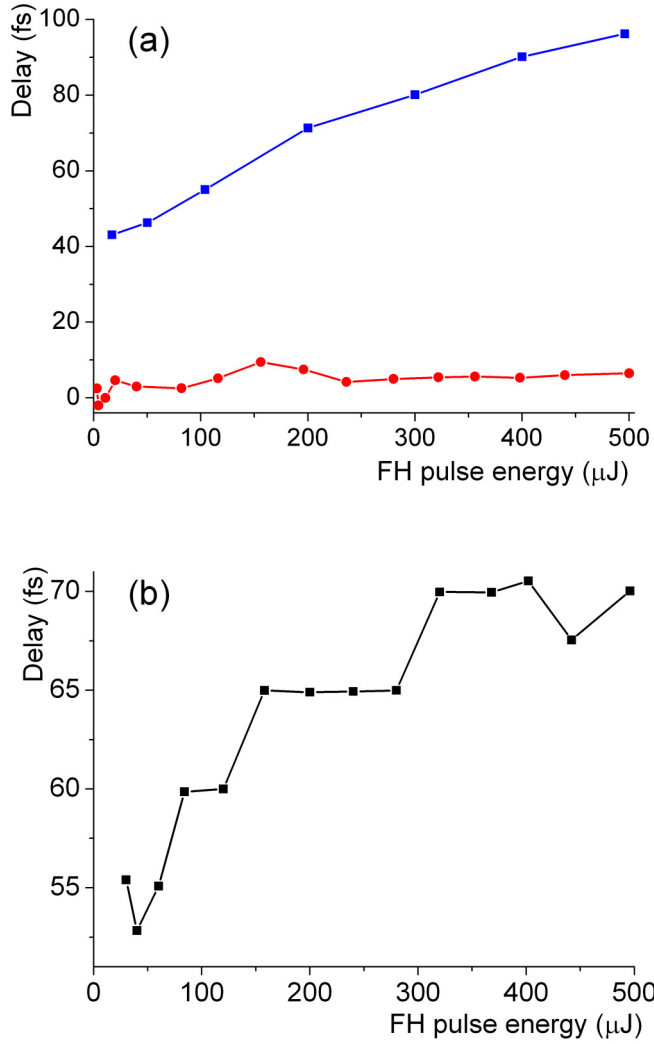


FIG. 5. Experimental results. Dependence of the temporal peak THG (a) and THz (b) signal position on the energy of FH pulses. In (a) the SH pulse energies were 1.5 mJ (red circles) and 14 μ J (blue squares). In (b) the SH pulse energy was 25 μ J. In (b), in order to enhance the THz yield FH and SH polarizations were set to be circular [11].

were observed also by varying FH power [compare Fig. 6(b) and its inset]; however, the effect was much weaker due to much lower maximal pulse energy and consequently shorter plasma filament length in comparison of that of the SH pulses.

III. NUMERICAL MODELING OF THz AND TH GENERATION BY THE TWO-COLOR PUMP

In order to explain the described effects, we present the numerical modeling. In the model, simplified experiment conditions are set, e.g., the FH and SH beams are linearly polarized and the focus lengths of both lenses are equal. Moreover, the beam radius is taken slightly smaller than the experimental one in order to overcome the time-consuming calculations. Therefore, the numerical results cannot be directly compared with the experimental results. However, qualitative agreement between the results is achieved and the experimentally observed effects can be explained.

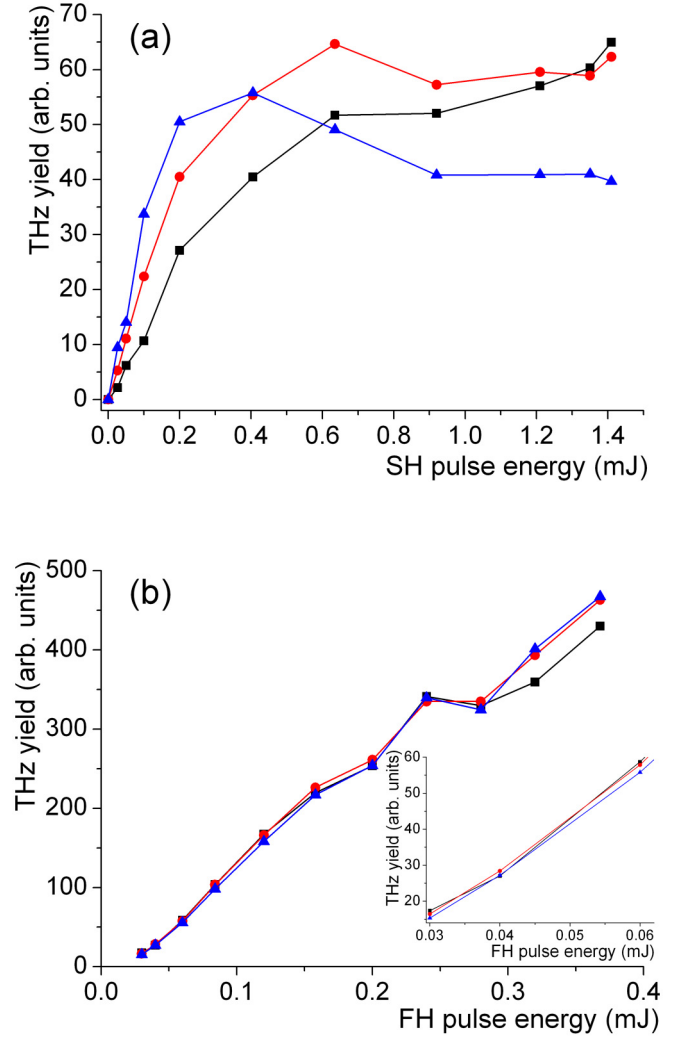


FIG. 6. Dependencies of the overall THz power on SH (a) and FH (b) pulse energies for the fixed delays between the FH and SH pulses. In (a) and (b) time delay increments are 15 and 5 fs, respectively.

A. Governing equations

We make use of the slowly evolving wave approximation for the nonlinear envelope equation [28]. Then, the nonlinear propagation of the THz, first harmonic, second harmonic, and third harmonic is described by the governing equations

$$\frac{\partial \hat{\mathcal{E}}_0}{\partial z} = iK_{0z} \hat{\mathcal{E}}_0 + \hat{\mathcal{P}}_0^{(3)} + \hat{\mathcal{P}}_0^{(pl)}, \quad (1)$$

$$\frac{\partial \hat{\mathcal{E}}_1}{\partial z} = iK_{1z} \hat{\mathcal{E}}_1 + \hat{\mathcal{P}}_1^{(3)} + \hat{\mathcal{P}}_1^{(pl)}, \quad (2)$$

$$\frac{\partial \hat{\mathcal{E}}_2}{\partial z} = iK_{2z} \hat{\mathcal{E}}_2 + \hat{\mathcal{P}}_2^{(3)} + \hat{\mathcal{P}}_2^{(pl)}, \quad (3)$$

$$\frac{\partial \hat{\mathcal{E}}_3}{\partial z} = iK_{3z} \hat{\mathcal{E}}_3 + \hat{\mathcal{P}}_3^{(3)} + \hat{\mathcal{P}}_3^{(pl)}, \quad (4)$$

where $\hat{\mathcal{E}}_{0,1,2,3}(\Omega, \beta_x, \beta_y, z)$ stands for the Fourier transform of the THz (index 0), FH (index 1), SH (index 2) and TH (index 3) envelopes $\mathcal{E}_{0,1,2,3}(t, x, y, z)$. z is the propagation distance, x

and y are the transverse coordinates, and t is time. $\Omega = \omega - \omega_{j0}$, where $\omega_{j0} = 2\pi c/\lambda_{j0}$ is the central cyclic frequency of the j th wave ($j = 0, 1, 2, 3$) and ω is the cyclic frequency. λ_{j0} is the central wavelength and c is the speed of light.

B. Dispersion and diffraction

The first right-hand side term in Eqs. (1)–(4) describes the free-space propagation in air. $K_{0,1,2,3z}$ is the shifted z projection of the wave vector, e.g., $K_{1,2,3z} = k_{1,2,3}(\omega) - \kappa_{1,2,3}(\omega) - (\beta_x^2 + \beta_y^2)/(2k_{1,2,30})$, $K_{0z} = \sqrt{k_0^2(\omega) - (\beta_x^2 + \beta_y^2)} - \kappa_0(\omega)$, where $\kappa_{0,1,2,3}(\omega) = k_{0,1,2,30} + (\omega - \omega_{0,1,2,30})/u_{10}$ and u_{10} is the group velocity of the fundamental wave in air. $k(\omega) = \omega n(\lambda)/c$, $\lambda = 2\pi c/\omega$ is the wavelength, and n is the wavelength dependent refractive index found by the use of the Sellmeier equations for air [29]. $k_{0,1,2,30}$ is the wave number at the central frequency $\omega_{0,1,2,30}$. The shift $(\omega - \omega_{0,1,2,30})/u_{10}$ means that the fields are described in the reference frame of the FH pulse.

C. Third-order nonlinearity

The nonlinear terms are given by

$$\widehat{P}_0^{(3)} = (0 + \Omega)(i\widehat{P}^{(\text{THz})}), \quad (5)$$

$$\widehat{P}_1^{(3)} = (\omega_{10} + \Omega)(i\widehat{P}_{\text{Kerr},1} + i\widehat{P}^{(a)}), \quad (6)$$

$$\widehat{P}_2^{(3)} = (\omega_{20} + \Omega)(i\widehat{P}_{\text{Kerr},2} + i\widehat{P}^{(b)}), \quad (7)$$

$$\widehat{P}_3^{(3)} = (\omega_{30} + \Omega)(i\widehat{P}_{\text{Kerr},3} + i\widehat{P}^{(c)}). \quad (8)$$

Here, $\widehat{P}_{\text{Kerr}}$, includes self- and cross-phase modulations. It is the Fourier transform of the following expressions:

$$P_{\text{Kerr},1} = \frac{1}{c}n_2(I_1 + 2I_2 + 2I_3)\mathcal{E}_1, \quad (9)$$

$$P_{\text{Kerr},2} = \frac{1}{c}n_2(I_2 + 2I_1 + 2I_3)\mathcal{E}_2, \quad (10)$$

$$P_{\text{Kerr},3} = \frac{1}{c}n_2(I_3 + 2I_1 + 2I_2)\mathcal{E}_3, \quad (11)$$

where n_2 is the nonlinear refractive index of air. $I_j = \frac{c\epsilon_0}{2}|\mathcal{E}_j|^2$ is the intensity ($j = 1, 2, 3$), and ϵ_0 is the vacuum permittivity.

$\widehat{P}^{(\text{THz})}$ is the generation term of the THz radiation. It is the Fourier transforms of $\frac{1}{c}n_2\frac{c\epsilon_0}{2}2\text{Re}\{\mathcal{E}_1^2\mathcal{E}_2^*\exp(i[2k_{10} - k_{20}]z)\}$, where $\text{Re}(\bullet)$ denotes the real part.

$\widehat{P}^{(a)}$, $\widehat{P}^{(b)}$, and $\widehat{P}^{(c)}$ are the Fourier transforms of $\frac{1}{c}n_2\frac{c\epsilon_0}{2}\{\mathcal{E}_3\mathcal{E}_1^{*2}\exp(i[k_{30} - 3k_{10}]z) + \mathcal{E}_2^2\mathcal{E}_3^*\exp(i[2k_{20} - k_{10} - k_{30}]z)\}$, $\frac{1}{c}n_2\frac{c\epsilon_0}{2}\mathcal{E}_1\mathcal{E}_3\mathcal{E}_2^*\exp(i[k_{10} + k_{30} - 2k_{20}]z)$, and $\frac{1}{c}n_2\frac{c\epsilon_0}{2}\{\frac{\mathcal{E}_1^3}{3}\exp(i[3k_{10} - k_{30}]z) + \mathcal{E}_2^2\mathcal{E}_1^*\exp(i[2k_{20} - k_{10} - k_{30}]z)\}$, respectively. The last term generates the third harmonic due to the $\chi^{(3)}$ nonlinearity.

D. Plasma density

The plasma density generation is described by the dynamic equation

$$\frac{\partial \rho^{(n)}}{\partial t} = [1 - \rho^{(n)}(t)]W(t), \quad (12)$$

TABLE I. MPI-model parameters at wavelengths $\lambda_{10} = 0.8 \mu\text{m}$, $\lambda_{20} = 0.4 \mu\text{m}$, and $\lambda_{30} = 0.267 \mu\text{m}$.

Parameter	Value	Units
K_{1O}	8	
K_{2O}	4	
K_{3O}	3	
Γ_{1O}	$10^{-124.4}$	$(\text{m}^2/\text{W})^8 \text{s}^{-1}$
Γ_{2O}	$10^{-55.0}$	$(\text{m}^2/\text{W})^4 \text{s}^{-1}$
Γ_{3O}	$10^{-37.5}$	$(\text{m}^2/\text{W})^3 \text{s}^{-1}$
K_{1N}	11	
K_{2N}	6	
K_{3N}	4	
Γ_{1N}	$10^{-180.4}$	$(\text{m}^2/\text{W})^{11} \text{s}^{-1}$
Γ_{2N}	$10^{-93.2}$	$(\text{m}^2/\text{W})^6 \text{s}^{-1}$
Γ_{3N}	$10^{-57.3}$	$(\text{m}^2/\text{W})^4 \text{s}^{-1}$

where $\rho^{(n)}$ is the normalized to the neutral density ρ_0 plasma density and $W(t)$ is the generation rate. Here, we use the MPI model. In this model,

$$W(t) = \sum_{j=1,2,3} [0.2\Gamma_{jO}I^{K_{jO}} + 0.8\Gamma_{jN}I^{K_{jN}}]. \quad (13)$$

The plasma is generated by FH ($j = 1$), SH ($j = 2$), and TH ($j = 3$). Two main constituents of air—oxygen (O) and nitrogen (N)—are taken into account. Γ coefficients were calculated by the use of the Ammosov-Delone-Krainov (ADK) formula taken from [30] (in [30], the misprints were corrected). The intensity dependence of the rate was fitted by a line in the logarithmic scale and Γ was found (see also [21] for more details). K is the photon number needed for the multiphoton ionization. The coefficients are given in Table I.

E. Plasma term

MPI model

In Eqs. (1)–(4) the plasma terms read

$$\widehat{P}_0^{(\text{pl})} = -i\text{FT}\left[\frac{q_e^2}{2m_e c \epsilon_0}\rho\mathcal{E}_0\right]\frac{1}{\Omega + i\gamma}, \quad (14)$$

$$\widehat{P}_1^{(\text{pl})} = -i\text{FT}\left[\frac{q_e^2}{2m_e c \epsilon_0}\rho\mathcal{E}_1\right]\frac{1}{\omega_1 + i\gamma} - J_{\text{loss},1}, \quad (15)$$

$$\widehat{P}_2^{(\text{pl})} = -i\text{FT}\left[\frac{q_e^2}{2m_e c \epsilon_0}\rho\mathcal{E}_2\right]\frac{1}{\omega_2 + i\gamma} - J_{\text{loss},2}, \quad (16)$$

$$\widehat{P}_3^{(\text{pl})} = -i\text{FT}\left[\frac{q_e^2}{2m_e c \epsilon_0}\rho\mathcal{E}_3\right]\frac{1}{\omega_3 + i\gamma} - J_{\text{loss},3}, \quad (17)$$

where $\text{FT}[\circ]$ denotes the Fourier transform and $\omega_j = \omega_{j0} + \Omega$. q_e and m_e are the electron charge and mass, respectively. Here, $\gamma = 1/200 \text{ fs}^{-1}$ stands for the absorption rate. The nonlinear loss terms at the multiphoton ionization are given by

$$J_{\text{loss},1} = \text{FT}\left[\frac{1}{2}\mathcal{E}_1\rho_0(0.2K_{1O}\hbar\omega_{10}\Gamma_{1O}I_1^{K_{1O}-1} + 0.8K_{1N}\hbar\omega_{10}\Gamma_{1N}I_1^{K_{1N}-1})\right], \quad (18)$$

$$J_{\text{loss},2} = \text{FT}\left[\frac{1}{2}\mathcal{E}_2\rho_0(0.2K_{2O}\hbar\omega_{20}\Gamma_{2O}I_2^{K_{2O}-1} + 0.8K_{2N}\hbar\omega_{20}\Gamma_{2N}I_2^{K_{2N}-1})\right], \quad (19)$$

$$J_{\text{loss},3} = \text{FT} \left[\frac{1}{2} \mathcal{E}_3 \rho_0 (0.2 K_{30} \hbar \omega_{30} \Gamma_{30} I_3^{K_{30}-1} + 0.8 K_{3N} \hbar \omega_{30} \Gamma_{3N} I_3^{K_{3N}-1}) \right]. \quad (20)$$

F. The input FH and SH pulsed beams

We assume no THz and TH at the input and the FH with SH is focused by a lens with the focus length f placed at $z = 0$. Then, at $z = 0$, the boundary conditions read

$$\mathcal{E}_1(t, x, y, z = 0) = E_0 \exp \left(-(x^2 + y^2) \left[\frac{1}{r_0^2} + \frac{i\pi}{\lambda_{10} f} \right] \right) \exp \left(-\frac{t^2}{\tau^2} \right), \quad (21)$$

$$\begin{aligned} \mathcal{E}_2(t, x, y, z = 0) &= E_0 \sqrt{m_2} \exp \left(-(x^2 + y^2) \left[\frac{1}{0.9^2 r_0^2} + \frac{2i\pi}{\lambda_{10} f} \right] \right) \\ &\times \exp \left(-\frac{(t - \Delta)^2}{\tau^2} \right) \end{aligned} \quad (22)$$

where r_0 is beam radius and τ is the pulse duration and Δ is the time delay. E_0 is the peak amplitude of the FH and $m_2 = |\mathcal{E}_{2,\text{max}}|^2 / |\mathcal{E}_{1,\text{max}}|^2$ is the ratio of the maximum intensities of the SH and FH at $z = 0$. Similarly as in experiment, the SH beam radius is 10% smaller than the radius of the FH.

We note that the parameter Δ in Eq. (22) is of the opposite sign with respect to the “delay” in the experimental part.

G. Numerical results

Equations (1)–(4) were simulated at following input parameters: $\lambda_1 = 0.8 \mu\text{m}$, $\tau = 30 \text{ fs}$, $r_0 = 4 \text{ mm}$ (about 5 mm at FWHM), $f = 15 \text{ cm}$. The cylindrical symmetry was assumed and the fast Hankel transform for the space domain was implemented [31]. The space domain $[0, 2r_0]$ was divided into 1500 parts and the time domain $[-8\tau_0, 8\tau_0]$ was divided into 64 equal parts. We used the Euler integration scheme. To save computation time, the longitudinal spatial step h_z was not uniform: in the vicinity of the focus $h_z = 0.75 \mu\text{m}$ and $h_z = 300 \mu\text{m}$ elsewhere. We define the vicinity of the focus as $0.96 \times f < z < 1.01 \times f$. Moreover, Eqs. (1)–(4) of the form $\frac{\partial \mathcal{E}}{\partial z} = iK\mathcal{E} + \hat{N}$ were rewritten in the form $\frac{\partial \mathcal{E}'}{\partial z} = \exp(-iKz)\hat{N}$, where $\mathcal{E}' = \mathcal{E} \exp(iKz)$ and \hat{N} is the nonlinear part.

Input energy of SH was fixed and amplitude of FH E_0 was varied. Hence, the factor m_2 in Eq. (22) was varied, too. We denote the starting FH energy value as $\eta_0 = 3.3 \mu\text{J}$ and afterwards increase it by the factors of 4 and 16. The SH intensity coincides with the FH intensity at energy η_0 . In the numerical simulations, the energy value of $\eta_0 = 3.3 \mu\text{J}$ corresponds to the onset of the FH filament formation (see Fig. 7). For the given FH energy values we have calculated the dependencies of the THz output energies on the time delay (Fig. 8). Here, we obtain the maxima of the curves at around $\Delta = 0 \text{ fs}$ for FH energy η_0 and at around $-\Delta = 20 \text{ fs}$ at FH energy $16\eta_0$.

To give insight into the reason for this maximum shift, we present Fig. 9 where the dependences of the FH and SH intensities and their maximum on-axis position on the propagation

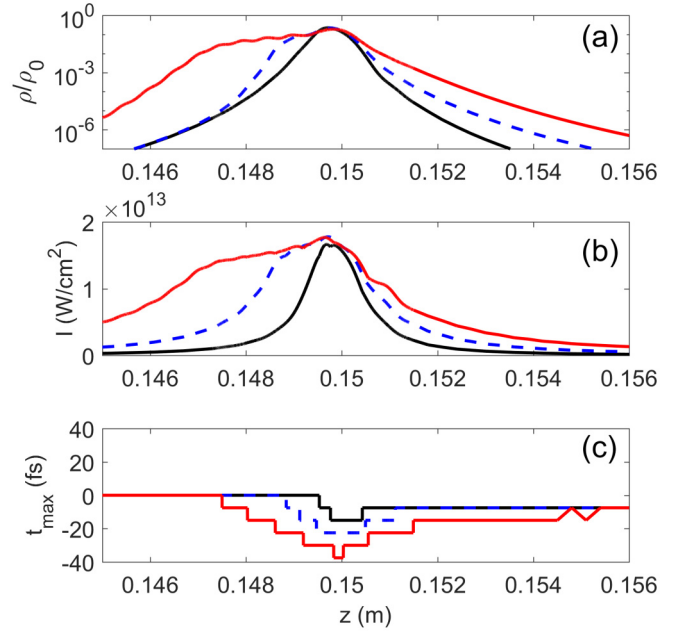


FIG. 7. Numerical results. Dependence of (a) plasma density, (b) FH intensity, and (c) the on-axis time position of the maximum intensity on the propagation distance in the vicinity of the lens focus. Input FH energy: $\eta_0 = 3.3 \mu\text{J}$ (black solid line), $4\eta_0$ (blue dashed line), and $16\eta_0$ (red solid line). $\Delta = 0 \text{ fs}$. (Here, the propagation takes place from the left to the right.)

distance are depicted. The most efficient THz generation is achieved when FH and SH pulses overlap at the lens focus. We note that in air the SH pulse propagates slower than the FH pulse. So, at $\Delta = 0 \text{ fs}$ the SH pulse falls behind the FH pulse when reaching the focus (by around 12 fs); see solid lines in Fig. 9(b). When approaching the focus, the intensity maximum position takes a dip, and the larger the input intensity or energy (e.g., the longer the filament) the larger the dip [Fig. 7(c)]. Thus, in order to obtain better overlap between

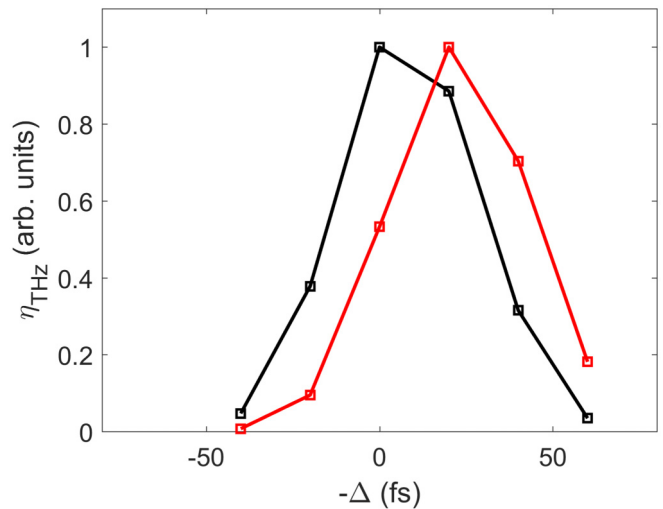


FIG. 8. Numerical results. Dependence of the output THz energy on the time delay. Input FH energy: $\eta_0 = 3.3 \mu\text{J}$ (black squares) and $16\eta_0 = 0.053 \text{ mJ}$ (red squares).

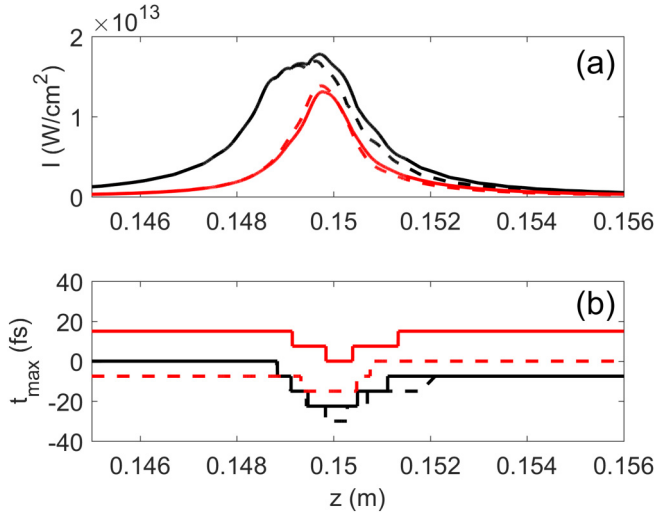


FIG. 9. Numerical results. Dependence of the FH (black lines) and SH (red lines) (a) intensity and (b) its maximum on-axis time position on the propagation distance. $\Delta = 0$ fs (solid lines) and $-\Delta = 20$ fs (dashed lines). FH input energy: $4\eta_0 = 13.2 \mu\text{J}$.

the FH and SH pulses, at larger input intensity the initial time delay should be larger. To compare better and worse overlaps of FH and SH as well as corresponding THz and TH yields, we depict the FH and SH pulse profiles at the focus in Fig. 10 and present the output THz and TH spectra in Fig. 11.

IV. DISCUSSION

The experimentally observed findings can be explained with the help of the numerical simulation results. The shift of the plasma filament onset towards the lens was observed both in experiment (Fig. 2) and in theory (Fig. 7). This shift is caused by the onset of the intensity clamping. The clamping starts before the focus when the input energy is sufficiently high. We note that in our numerical simulations the self-focusing is not crucial. For FH Gaussian beams, critical

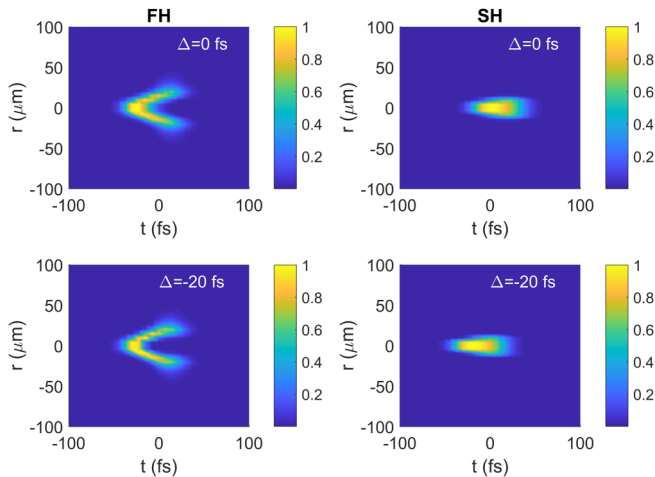


FIG. 10. Numerically calculated FH and SH intensity profiles at the focus. FH input energy: $4\eta_0 = 13.2 \mu\text{J}$. Pulses propagate towards the negative time.

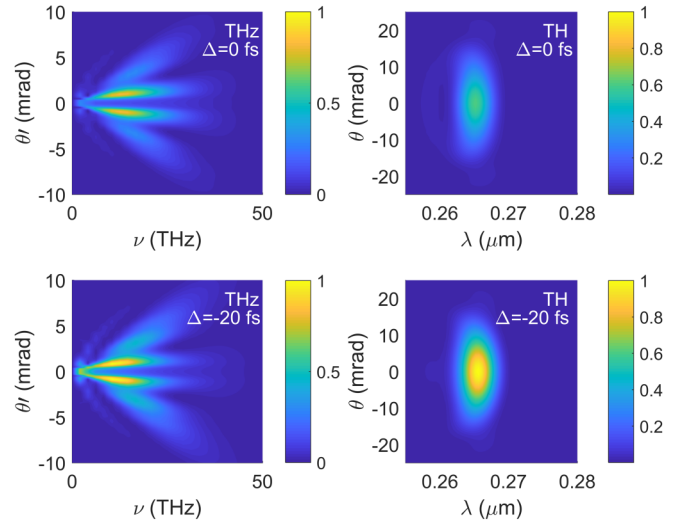


FIG. 11. Numerically calculated output spectra of THz and TH radiation. FH input energy: $4\eta_0 = 13.2 \mu\text{J}$. Here, $\theta = \sqrt{\beta_x^2 + \beta_y^2}/k_{30}$ is the angle while $\theta' = \sqrt{\beta_x^2 + \beta_y^2}/k_{10}$ is a parameter not representing the real angle. The THz angle $\theta_{\text{THz}} = \frac{\nu_0}{\nu}\theta'$, where $\nu_0 = 375$ THz is the FH frequency and ν is the frequency of the THz radiation.

power is calculated from [28]: $P_{\text{cr}} = 3.77\pi n(\lambda_1)/(2k_1^2 n_2)$. At $n_2 = 4 \times 10^{-23} \text{ m}^2/\text{W}$, we find $P_{\text{cr}} = 2.4$ GW. In our case, at an energy of 1 mJ, the input power $P = 19$ GW and the self-focusing distance is given by [25]:

$$z_c = \frac{0.367z_R}{\{[(P/P_{\text{cr}})^{1/2} - 0.852]^2 - 0.0219\}^{1/2}}. \quad (23)$$

Here, the diffraction length $z_R = k_1 r_0^2/2$. We find $z_R = 63$ m and $z_c = 12$ m. We note that in this case the focus length of the lens is much smaller (15 cm) than the self-focusing distance (12 m) and the net focus length given by $f' = fz_c/(f + z_c)$ is equal to 0.148 m. Then, the focus shift [25] is of 2 mm. However, in our numerical simulations the largest power is 1 GW and then the self-focusing does not take place. We note that we use the term ‘‘filament’’ since the estimated Rayleigh length $\frac{8\lambda_1}{\pi} \left(\frac{f}{2r_0}\right)^2 = 0.7$ mm usually is smaller than the plasma filament length [several mm, Fig. 7(b), red line].

The cross-correlation functions of FH and SH were both measured (Fig. 4) and calculated (Fig. 8). When the SH energy is low, the correlation maximum shifts to larger delay values with FH input energy [see also Fig. 5 (blue and black lines)]. This effect is explained by the numerically observed dip in the maximum-time curve [Fig. 9(b)]. The generated plasma defocuses the back of the pulse (Fig. 10) so that the pulse maximum shifts toward the leading part of the pulse (e.g., negative time values). This shift becomes larger when the filament is longer [Fig. 7(c)] and then the delay between the FH and SH should increase. A longer filament means a longer plasma channel [Figs. 7(a) and 7(b)], so the correlation measurements may provide the characterization of the plasma channel length.

When SH pulse energy is much larger than that of the FH, the filament is formed mainly by the SH and the increase of the FH energy is not crucial. Then, the correlation maximum is fixed [see red line in Fig. 5(a)].

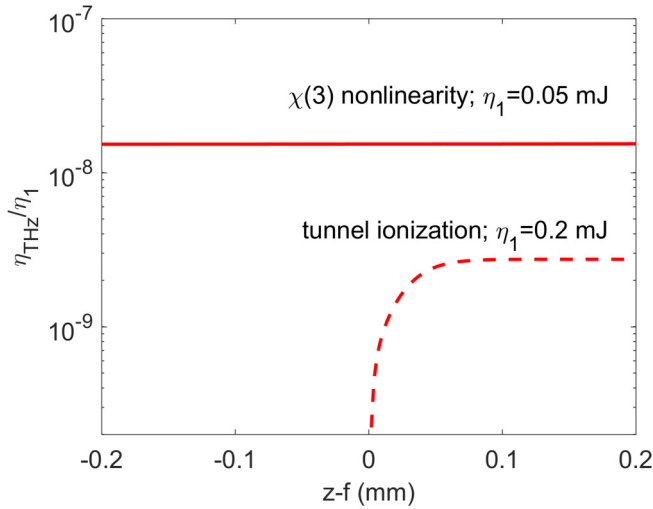


FIG. 12. Numerical results. Comparison of the impacts of $\chi^{(3)}$ nonlinearity [solid line, Eqs. (1)–(4)] and plasma current [dashed line, Eq. (A1)] to the THz yield.

Although the typical THz output spectra are ring shaped while the TH beam is mainly axially directed (Fig. 11) the delay shifts of the correlation functions are qualitatively similar in both cases [compare blue and black lines in Figs. 5(a) and 5(b)]. We note that the third harmonic is generated also in the absence of the SH beam while the THz generation is determined by the overlap of the FH and SH beams. Therefore, finding conditions of the FH and SH overlap is more important in the case of THz generation. On the other hand, the observed time shifts could take place during other nonlinear optical processes, such as parametric four-wave mixing and generation [4,32–34], i.e., whenever the femtosecond bichromatic pump beams are used and laser-induced plasma is created.

Finally, the described numerical simulations were performed assuming that the terahertz radiation is generated only by the $\chi^{(3)}$ nonlinearity of the medium and the plasma ionization is driven only by the multiphoton ionization mechanism. In the strong field of the pump wave this assumption is not correct [13,14] since then the main impact to the generated THz radiation is created by the plasma currents and is provided by the tunnel ionization. Therefore, we need to check if at the onset of the intensity clamping the plasma-current contribution is not significant with respect to the $\chi^{(3)}$ nonlinearity. We utilized the model equation given in the Appendix [Eq. (A1)] that omits the $\chi^{(3)}$ nonlinear terms but takes into account the tunnel ionization. The input FH and SH waves were Gaussian beams with beam diameter $2r_0 = 10 \mu\text{m}$ and pulse durations $\tau = 30 \text{ fs}$. Ideal overlapping was assumed, $\Delta = 0 \text{ fs}$. The propagation was simulated from the coordinate $z = 0$ to 0.2 mm . In the simulation, the time interval $[-8\tau_0, 8\tau_0]$ was divided into 8192 equal parts and the space domain $[0, 2r_0]$ was divided into 100 parts. The results are presented in Fig. 12 where the numerically obtained THz yields are compared. Here, in the model equation with tunnel ionization we set the input intensity $I = 1.5 \times 10^{13} \text{ W/cm}^2$. This value corresponds to the clamped intensity [Fig. 7(b)], and an energy of 0.2 mJ . This energy value is higher than the

highest value in the numerical simulations with multiphoton ionization and $\chi^{(3)}$ nonlinearity ($16 \times 3.3 \mu\text{J} = 0.05 \text{ mJ}$). However, in this case, the $\chi^{(3)}$ impact to the THz yield is higher than the plasma-current impact (Fig. 12).

V. CONCLUSIONS

In conclusion, the yield of third-harmonic and terahertz radiation generation in air by bichromatic femtosecond laser pulses has been investigated both numerically and experimentally as a function of the delay between the laser pulses, i.e., the correlation functions of the fundamental and second harmonics were analyzed at various pump powers. We have demonstrated that the maxima of measured and numerically calculated correlation functions shift with the increase of the input energy. The reason for this shift is the plasma-assisted time shift of the pulse maximum in the vicinity of the focus. Therefore, the THz yield can be enhanced by the appropriate initial time delay between the fundamental and second harmonics. Moreover, the generated plasma channel length can be characterized using the measured THz or TH correlation functions.

ACKNOWLEDGMENT

This research was funded by a grant (Grant No. S-MIP-19-46) from the Lietuvos Mokslo Taryba (Research Council of Lithuania).

APPENDIX: MODEL EQUATION WITH TUNNEL IONIZATION

The model equation accounting for the tunnel ionization is an unidirectional pulse propagation equation written for the Fourier transform $\hat{E}(\omega, \beta_x, \beta_y, z)$ of the field $E(t, x, y, z)$ in the local fundamental pulse frame [28]:

$$\frac{\partial \hat{E}}{\partial z} = iK_z \hat{E} - (\hat{P}'_{\text{loss}} + i\hat{P}'_e), \quad (\text{A1})$$

where $K_z = \sqrt{k^2(\omega) - \beta_x^2 - \beta_y^2} - \omega/u_{10}$ is the shifted z projection of the wave number. Here, only the plasma nonlinear terms are taken into account, omitting the $\chi^{(3)}$ nonlinearity. Plasma density is estimated from Eq. (12) with the rate describing the tunnel ionization [22]:

$$W_U = \frac{\alpha E_a}{|E|} \exp\left(-\frac{\beta E_a}{|E|}\right), \quad (\text{A2})$$

where $E_a \approx 5.14 \times 10^{11} \text{ V/m}$ is the atomic electric field, coefficients $\alpha = 4\omega_a r_H^{5/2}$ and $\beta = \frac{2}{3} r_H^{3/2}$, and the ratio $r_H = U/U_H$. $U_H = 13.6 \text{ eV}$ is the ionization potential of hydrogen and $\omega_a \approx 4.13 \times 10^{16} \text{ s}^{-1}$. We calculate W_U both with the oxygen ionization potential $U = U_O$ and with the nitrogen ionization potential $U = U_N$. Then, the whole rate is given by $W(t) = 0.2W_{U_O} + 0.8W_{U_N}$. The plasma current term is given by $\hat{P}'_e = \frac{1}{\omega + i\gamma} \text{FT}\left[\frac{q_e^2}{2m_e c \epsilon_0} \rho E\right]$ and the nonlinear losses are described by $\hat{P}'_{\text{loss}} = \frac{1}{2} \sqrt{\frac{\mu_0}{\epsilon_0}} \text{FT}[(0.2W_{U_O}U_O + 0.8W_{U_N}U_N)(\rho_0 - \rho)/E]$.

- [1] C. Rodríguez, Z. Sun, Z. Wang, and W. Rudolph, Characterization of laser-induced air plasmas by third harmonic generation, *Opt. Express* **19**, 16115 (2011).
- [2] G. O. Ariunbold, P. Polynkin, and J. V. Moloney, Third and fifth harmonic generation by tightly focused femtosecond pulses at 2.2 μm wavelength in air, *Opt. Express* **20**, 1662 (2012).
- [3] V. Vaičaitis, Cherenkov-type phase-matched third harmonic generation in air, *Opt. Commun.* **185**, 197 (2000).
- [4] F. Théberge, N. Aközbek, W. Liu, A. Becker, and S. L. Chin, Tunable Ultrashort Laser Pulses Generated Through Filamentation in Gases, *Phys. Rev. Lett.* **97**, 023904 (2006).
- [5] V. Vaičaitis, V. Jarutis, K. Steponkevičius, and A. Stabinis, Noncollinear six-wave mixing of femtosecond laser pulses in air, *Phys. Rev. A* **87**, 063825 (2013).
- [6] F. Théberge, M. Châteauneuf, V. Ross, P. Mathieu, and J. Dubois, Ultrabroadband conical emission generated from the ultraviolet up to the far-infrared during the optical filamentation in air, *Opt. Lett.* **33**, 2515 (2008).
- [7] V. Vaičaitis, R. Butkus, O. Balachninaite, U. Morgner, and I. Babushkin, Diffraction-enhanced femtosecond white-light filaments in air, *Appl. Phys. B* **124**, 221 (2018).
- [8] S. L. Chin, S. Hosseini, W. Liu, Q. Luo, F. Théberge, N. Aközbek, A. Becker, V. Kandidov, O. Kosareva, and H. Schroeder, The propagation of powerful femtosecond laser pulses in optical media: Physics, applications, and new challenges, *Can. J. Phys.* **83**, 863 (2005).
- [9] A. Couairon and A. Mysyrowicz, Femtosecond filamentation in transparent media, *Phys. Rep.* **441**, 47 (2007).
- [10] I. Babushkin, W. Kuehn, C. Köhler, S. Skupin, L. Bergé, K. Reimann, M. Woerner, J. Herrmann, and T. Elsaesser, Ultrafast Spatiotemporal Dynamics of Terahertz Generation by Ionizing Two-Color Femtosecond Pulses in Gases, *Phys. Rev. Lett.* **105**, 053903 (2010).
- [11] C. Tailliez, A. Stathopoulos, S. Skupin, D. Buožius, I. Babushkin, V. Vaičaitis, and L. Bergé, Terahertz pulse generation by two-color laser fields with circular polarization, *New J. Phys.* **22**, 103038 (2020).
- [12] D. Dietze, J. Darmo, S. Roither, A. Pugzlys, J. N. Heyman, and K. Unterrainer, Polarization of terahertz radiation from laser generated plasma filaments, *J. Opt. Soc. Am. B* **26**, 2016 (2009).
- [13] L. Bergé, S. Skupin, C. Köhler, I. Babushkin, and J. Herrmann, 3D Numerical Simulations of THz Generation by Two-Color Laser Filaments, *Phys. Rev. Lett.* **110**, 073901 (2013).
- [14] V. Andreeva, O. Kosareva, N. Panov, D. Shipilo, P. Solyankin, M. Esaulkov, P. González de Alaiza Martínez, A. Shkurinov, V. Makarov, L. Bergé, and S. Chin, Ultrabroad Terahertz Spectrum Generation from an Air-Based Filament Plasma, *Phys. Rev. Lett.* **116**, 063902 (2016).
- [15] Z. Zhang, N. Panov, V. Andreeva, Z. Zhang, A. Slepkov, D. Shipilo, M. D. Thomson, T.-J. Wang, I. Babushkin, A. Demircan, U. Morgner, Y. Chen, O. Kosareva, and A. Savel'ev, Optimum chirp for efficient terahertz generation from two-color femtosecond pulses in air, *Appl. Phys. Lett.* **113**, 241103 (2018).
- [16] K.-Y. Kim, J. H. Glowia, A. J. Taylor, and G. Rodriguez, Terahertz emission from ultrafast ionizing air in symmetry-broken laser fields, *Opt. Express* **15**, 4577 (2007).
- [17] K. Y. Kim, A. J. Taylor, J. H. Glowia, and G. Rodriguez, Coherent control of terahertz supercontinuum generation in ultrafast laser interactions, *Nat. Photonics* **2**, 605 (2008).
- [18] J. Peñano, P. Sprangle, B. Hafizi, D. Gordon, and P. Serafim, Terahertz generation in plasmas using two-color laser pulses, *Phys. Rev. E* **81**, 026407 (2010).
- [19] I. Alexeev, A. C. Ting, D. F. Gordon, E. Briscoe, B. Hafizi, and P. Sprangle, Characterization of the third-harmonic radiation generated by intense laser self-formed filaments propagating in air, *Opt. Lett.* **30**, 1503 (2005).
- [20] H. Xu, H. Xiong, Y. Fu, J. Yao, Z. Zhou, Y. Cheng, Z. Xu, and S. L. Chin, Formation of X-waves at fundamental and harmonics by infrared femtosecond pulse filamentation in air, *Appl. Phys. Lett.* **93**, 241104 (2008).
- [21] V. Tamulienė, G. Juškevičiūtė, D. Buožius, V. Vaičaitis, I. Babushkin, and U. Morgner, Influence of tunnel ionization to third-harmonic generation of infrared femtosecond laser pulses in air, *Sci. Rep.* **10**, 17437 (2020).
- [22] I. Babushkin, C. Brée, C. M. Dietrich, A. Demircan, U. Morgner, and A. Husakou, Terahertz and higher-order Brunel harmonics: From tunnel to multiphoton ionization regime in tailored fields, *J. Mod. Opt.* **64**, 1078 (2017).
- [23] Y. Cheng, H. Xie, Z. Wang, G. Li, B. Zeng, F. He, W. Chu, J. Yao, and L. Qiao, Onset of nonlinear self-focusing of femtosecond laser pulses in air: Conventional vs spatiotemporal focusing, *Phys. Rev. A* **92**, 023854 (2015).
- [24] F. Théberge, W. Liu, P. T. Simard, A. Becker, and S. L. Chin, Plasma density inside a femtosecond laser filament in air: Strong dependence on external focusing, *Phys. Rev. E* **74**, 036406 (2006).
- [25] W. Liu and S. L. Chin, Direct measurement of the critical power of femtosecond Ti:sapphire laser pulse in air, *Opt. Express* **13**, 5750 (2005).
- [26] D. J. Cook and R. M. Hochstrasser, Intense terahertz pulses by four-wave rectification in air, *Opt. Lett.* **25**, 1210 (2000).
- [27] V. Vaičaitis, M. Ivanov, K. Adomavičius, Ž. Svirskas, U. Morgner, and I. Babushkin, Influence of laser-preformed plasma on THz wave generation in air by bichromatic laser pulses, *Laser Phys.* **28**, 095402 (2018).
- [28] A. Couairon, E. Brambilla, T. Corti, D. Majus, O. de J. Ramírez-Góngora, and M. Kolesik, Practitioners guide to laser pulse propagation models and simulation, *Eur. Phys. J. Spec. Top.* **199**, 5 (2011).
- [29] P. E. Ciddor, Refractive index of air: New equations for the visible and near infrared, *Appl. Opt.* **35**, 1566 (1996).
- [30] F. A. Ilkov, J. E. Decker, and S. L. Chin, Ionization of atoms in the tunnel regime with experimental evidence using Hg atoms, *J. Phys. B* **25**, 4005 (1992).
- [31] P. Banerjee, G. Nehmetallah, and M. Chatterjee, Numerical modeling of cylindrically symmetric nonlinear self-focusing using an adaptive fast Hankel split-step method, *Opt. Commun.* **249**, 293 (2005).
- [32] T. Fuji and T. Suzuki, Generation of sub-two-cycle mid-infrared pulses by four-wave mixing through filamentation in air, *Opt. Lett.* **32**, 3330 (2007).
- [33] V. Vaičaitis and A. Piskarskas, Tunable four-photon picosecond optical parametric oscillator, *Opt. Commun.* **117**, 137 (1995).
- [34] E. Gaizauskas, D. Pentaris, T. Efthimiopoulos, and V. Vaičaitis, Probing electronic coherences by combined two- and one-photon excitation in atomic vapors, *Opt. Lett.* **38**, 124 (2013).